

Dual-Function, Tunable, Nitrogen-Doped Carbon for High-Performance Li Metal–Sulfur Full Cell

Hongyan Li, Zheng Cheng, Avi Natan, Ahmed M. Hafez, Daxian Cao, Yang Yang, and Hongli Zhu*

Lithium metal–sulfur (Li–S) batteries are attracting broad interest because of their high capacity. However, the batteries experience the polysulfide shuttle effect in cathode and dendrite growth in the Li metal anode. Herein, a bifunctional and tunable mesoporous carbon sphere (MCS) that simultaneously boosts the performance of the sulfur cathode and the Li anode is designed. The MCS homogenizes the flux of Li ions and inhibits the growth of Li dendrites due to its honeycomb structure with high surface area and abundance of nitrogen sites. The Li@MCS cell exhibits a small overpotential of 29 mV and long cycling performance of 350 h under the current density of 1 mA cm⁻². Upon covering one layer of amorphous carbon on the MCS (CMCS), an individual carbon cage is able to encapsulate sulfur inside and reduce the polysulfide shuttle, which improves the cycling stability of the Li–S battery. As a result, the S@CMCS has a maximum capacity of 411 mAh g⁻¹ for 200 cycles at a current density of 3350 mA g⁻¹. Based on the excellent performance, the full Li–S cell assembled with Li@MCS anode and S@CMCS cathode shows much higher capacity than a cell assembled with Li@Cu anode and S@CMCS cathode.

application of Li–S batteries still has many challenges.^[8] First, the final discharge product of sulfur is insulating, which reduces the reaction kinetics.^[9] Second, polysulfide dissolves in the electrolyte and then shuttles from the cathode side to the anode side, causing a serious capacity decay during charge and discharge.^[10] The above shortcomings will lead to low Coulombic efficiency (CE) and capacity attenuation. In addition, the volume expansion of sulfur during charge and discharge will damage the electrochemical stability of whole Li–S batteries, which limits their practical application.

Li metal anode is considered to have the greatest potential for next-generation batteries.^[11] However, since the 1990s, the dendrite formation and safety concerns have limited the application of Li metal anode.^[12] The nonuniform morphology of the solid electrolyte interface (SEI) layer causes unbalanced Li ion flux, which then results in the inhomogeneous deposition of Li ions.^[14] Typically, the dendrites continue to grow during repeated plating/stripping process, which leads to low Coulombic efficiency and shortened cycle life.^[13] Additionally, some Li dendrites may penetrate the separator and result in serious safety issues. Therefore, the most critical factor for the Li–S battery's commercialization is suppressing the Li dendrite growth, which improves the Coulombic efficiency and reduces safety concerns for long cycling.

Many researchers have focused on improving the issues of sulfur cathode and Li metal anode separately.^[15,16] However, for the commercial application, improving the sulfur cathode and Li anode must be simultaneously considered. Previously, there have been very few reports of using bifunctional materials to ameliorate the electrochemical capability of the cathode and anode. Herein, a mesoporous carbon sphere is reported (according to different pyrolysis temperature, denoted as MCS900 and MCS1100) that not only homogenizes the flux of Li ions through the abundant nitrogen groups on the sphere but also inhibits the Li dendrites' growth.^[16–18] When the outer surface of the sphere is covered with one layer of amorphous carbon (CMCS1100), the multiplicity of mesoporous structures acts as individual carbon cages and encapsulates sulfur inside.^[19] This feature reduces the polysulfide shuttle, improves


the cycling stability of the Li–S battery. As a result, the S@CMCS has a maximum capacity of 411 mAh g⁻¹ for 200 cycles at a current density of 3350 mA g⁻¹. Based on the excellent performance, the full Li–S cell assembled with Li@MCS anode and S@CMCS cathode shows much higher capacity than a cell assembled with Li@Cu anode and S@CMCS cathode.

1. Introduction

Electronics have become an indispensable part of society due to rapid economic growth and societal dependence, which means efficient, long-lasting batteries are critical for electronic devices.^[1,2] Because of their remarkable advantage in specific energy, lithium metal–sulfur (Li–S) batteries have drawn tremendous attention.^[3–5] The high specific energy comes from sulfur's high energy density (2600 Wh kg⁻¹) and theoretical capacity (1675 mAh g⁻¹)^[6] and Li metal's high theoretical capacity (3860 mAh g⁻¹) and low reduction potential (–3.04 V vs standard hydrogen electrode).^[7]

Although the sulfur cathode benefits from high capacity, low cost, eco-friendliness, and natural abundance, the practical

Dr. H. Li, Z. Cheng, A. Natan, A. M. Hafez, D. Cao, Dr. Y. Yang, Prof. H. Zhu
Department of Mechanical and Industrial Engineering
Northeastern University
Boston, MA 02115, USA
E-mail: h.zhu@neu.edu

 The ORCID identification number(s) for the author(s) of this article can be found under <https://doi.org/10.1002/sml.201804609>.

DOI: 10.1002/sml.201804609

the cycling stability of the full Li–S battery, and achieves the concept of dual functionality. When Cu foil covered with MCS900 as working electrode was used in the half cell test, the Coulombic efficiency was stable at 96% after 300 cycles under a current density of 1 mA cm^{-2} and 91% after 100 cycles under a current density of 3 mA cm^{-2} . Moreover, the Li@MCS900 cell achieved a long-life cycling performance of 350 h under the current density of 1 mA cm^{-2} . It also showed a minimal overpotential of 29 mV compared with Li@Cu cell. Remarkably, Li-deposited MCS900 (anode) and sulfur-loaded CMCS1100 (cathode) in one full Li–S cell demonstrate excellent capacity performance. Specifically, the capacity of the S@CMCS1100||Li@MCS900 cell revealed high stability at 360 mAh g^{-1} for 200 cycles under a high current density of 1675 mA g^{-1} (1 C), which is much better performance than the S@CMCS1100||Li@Cu cell. This work establishes the possibility for developing a high-performance two-in-one material for Li–S batteries.

2. Results and Discussion

The preparation procedure of MCS and CMCS is schematically described in Figure 1a. The process starts from the

self-assembly of conductive polymer polyaniline (PANI) with colloidal SiO_2 . First, aniline and colloidal SiO_2 were mixed together to get a stable dispersion solution through sonication. Then ammonium persulfate was added into the solution to induce the polymerization reaction, forming composite PANI– SiO_2 nanospheres. The PANI– SiO_2 nanospheres have two functions: constructing the mesoporous carbon sphere (MCS) with open pore structure; and contributing to the formation of the closed pore structure (CMCS). After etching with NaOH solution, the SiO_2 template was removed and nitrogen-doped carbon spheres with mesoporous structure are fabricated (Figure 1a–I). During carbonization, the aromatic structure and high nitrogen content of PANI ensure that a large number of nitrogen atoms are uniformly doped into the carbon framework.^[20] Additionally, PANI– SiO_2 nanospheres with a hard template were successfully coated with a uniform and smooth layer of polydopamine (PDA) (Figure 1a–II).^[21] These core–shell PANI– SiO_2 @PDA nanocomposites are transformed into C– SiO_2 @C after carbonization in N_2 atmosphere (at $1100 \text{ }^\circ\text{C}$). The SiO_2 core can be easily dissolved by NaOH to obtain carbon-covered MCS. Figure 1b,d and Figure S1 in the Supporting Information represent typical scanning electron microscopy (SEM) images for the MCS900 sample. The MCS is mainly composed of

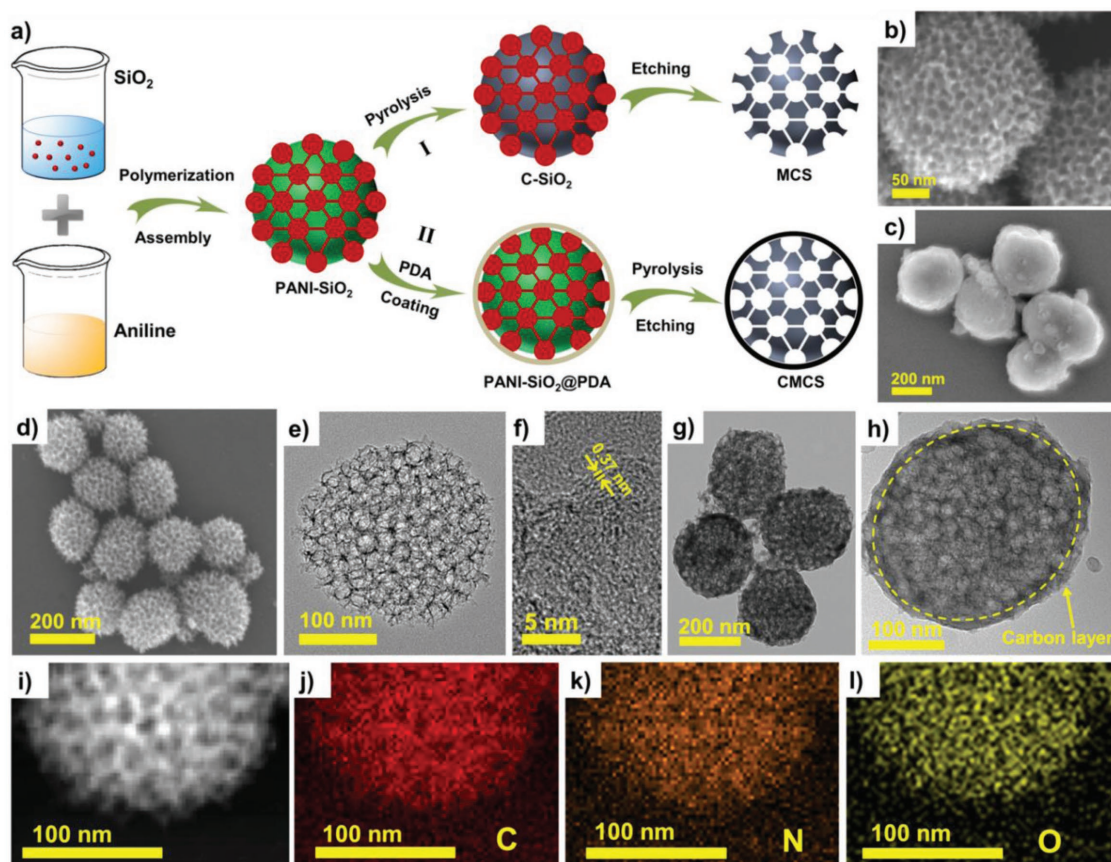


Figure 1. a) Schematic diagram of self-assembly of colloidal SiO_2 with conducting polymer PANI (PANI– SiO_2) and the steps to obtain the MCS and CMCS. b,d) SEM images of the prepared MCS900. c) SEM image of the prepared CMCS1100. e) TEM image of the prepared MCS900. f) HRTEM image of MCS900. g,h) TEM images of the prepared CMCS1100. HAADF-STEM and elemental mapping images of i) MCS900, j) carbon, k) nitrogen, and l) oxygen.

honeycomb-like concave surfaces of carbon spheres after etching the SiO₂. After annealing, PDA covered the PANI–SiO₂ precursor, as shown in Figure 1c. All of the exposed concave MCS structures were covered by a single carbon layer. The MCS with porous structure was further verified by transmission electron microscopy (TEM) image (Figure 1e). It is clearly observed that the MCS has an open porous morphology. During polymerization of PANI, the SiO₂ nanoparticles were uniformly embedded into the PANI. Then, the MCSs were fabricated after carbonization and etching treatment. From the high-resolution TEM (HRTEM) analysis, the MCS900 shows a disordered pattern with short-range order (Figure 1f). The interlayer spacing (d_{002}) was obtained as 0.37 nm, which is larger than that of graphite (0.33 nm).^[22] The independent unit of CMCS is further elucidated by TEM (Figure 1g,h). The hollow carbon cages not only store the sulfur, but also inhibit the shuttle of polysulfides during charge and discharge processes. Meanwhile, corresponding high-angle annular dark-field scanning transmission electron microscopy (HAADF-STEM) and elemental mapping images of C, N, and O of the MCS900 were investigated and shown in Figure 1i–l, which reveal the distributions of C, N, and O in the MCS900.

X-ray diffraction (XRD), Raman spectra, and X-ray photoelectron spectroscopy (XPS) were also used to further investigate the structure and composition of MCS1100 and MCS900. As shown in Figure 2a, two broad peaks at about 24.05° (d spacing of 3.69 Å) and 43.65° were observed from the XRD pattern of

MCS900, which correspond to the (002) and (100) planes of the graphitic carbon, respectively. However, compared with the (002) diffraction peak of the MCS900, the (002) diffraction peak of MCS1100 is shifted to 22.07°. The corresponding d spacing also increases to 4.02 Å. Raman spectra analysis was employed to further identify the degree of graphitization for the MCS1100 and MCS900. The intensity ratio of I_D to I_G is 0.83 for MCS900 and 0.86 for MCS1100, indicating that the MCS1100 and MCS900 materials both represent partial graphitization.^[20] XPS was used to analyze the chemical composition of MCS900. Three peaks appeared at 285, 400, and 530 eV, corresponding to C 1s, N 1s, and O 1s, respectively (Figure 2c). The oxygen species mainly come from the doping effect of oxygen in SiO₂ hard templates.^[23] The high-resolution N 1s spectrum of MCS900 can be divided into three different nitrogen species: pyridinic N (398.4 eV), pyrrolic N (399.8 eV), and quaternary N (400.9 eV). These nitrogen species would be beneficial to guide Li nucleation uniformly and further suppress the growth of Li dendrites.^[17,24,25]

The mechanism of Li deposition on Cu foil with and without MCS900 is illustrated in Figure 3a,b. The Cu foils are widely used as current collectors for Li metal anodes. However, the large protuberances on the Cu surface will cause large electric field distribution during the charging process.^[26] Hence, the Li ions will easily adsorb on the large protuberances, which leads to Li nucleation. The Li metal grows into Li dendrites under continuous preferential nucleation^[27] (Figure 3a). MCS900, with a large number of nitrogen sites on the honeycomb-like

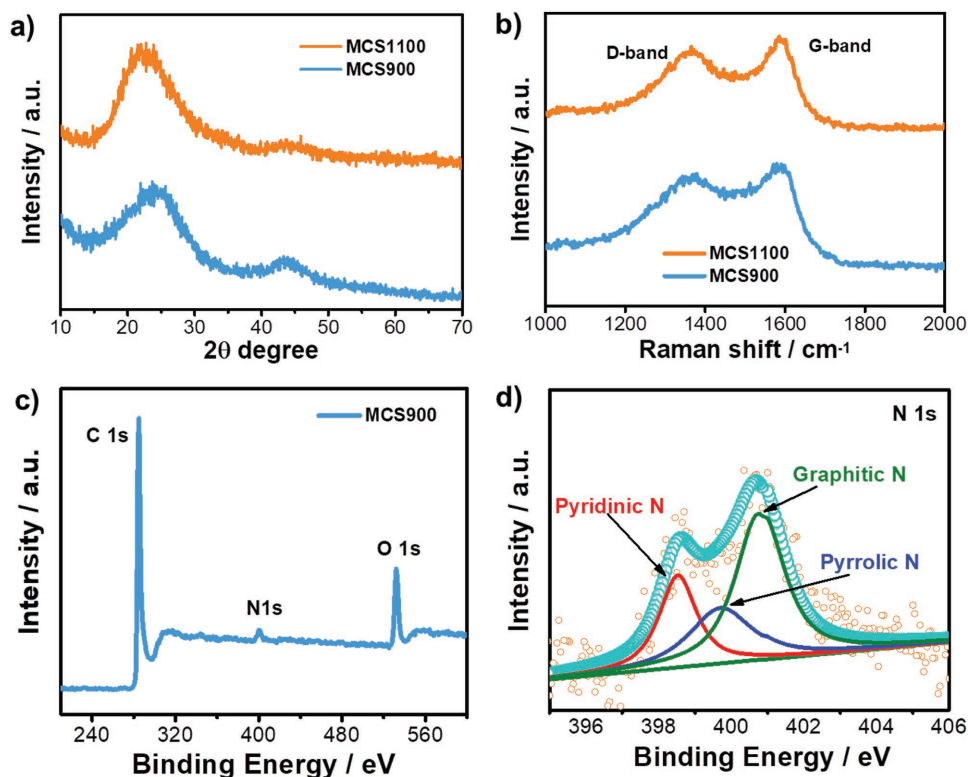


Figure 2. a) XRD patterns of MCS900 and MCS1100. b) Raman spectra of MCS900 and MCS1100. c) XPS survey spectra of MCS900. d) High-resolution N 1s spectrum of the N-doped MCS900.

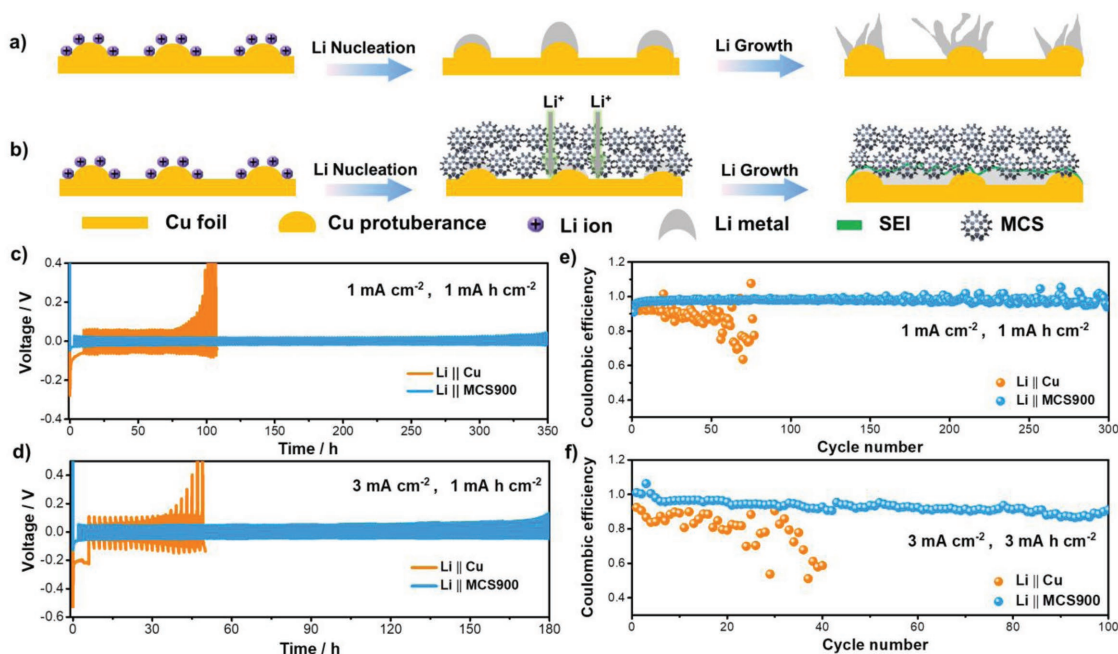


Figure 3. a,b) Schematic illustration of Li growth on Cu foil directly and through MCS900 material. c,d) Comparison of the cycling performance for Li plating/stripping on Cu electrode and the MCS900 electrode under current densities of 1 and 3 mA cm⁻². e,f) Comparison of the CE for Li plating/stripping on Cu electrode and the MCS900 electrode under current densities of 1 and 3 mA cm⁻².

structure, will effectively adjust the distribution of Li ions and create uniform deposition of Li ions^[24] (Figure 3b). In order to evaluate the voltage variation of Li during the plating/stripping process in cycling performance, the MCS900/Cu and bare Cu were compared as working electrode. The comparison of the voltage profiles for Li@MCS900 electrode and Li@Cu electrode at 1 mA cm⁻² (1 mAh cm⁻²) is presented in Figure 3c. Remarkably, the Li@MCS900 cell exhibited long cycling performance of 350 h. It also shows a small overpotential of 29 mV compared with the Li@Cu cell (Figure S2a, Supporting Information). The MCS900 electrode presents a stable voltage profile, which is attributed to the uniform distribution of Li ion flux and the stabilization of SEI formation. However, the Li@Cu electrode showed a larger overpotential of 93 mV and an unstable voltage profile (Figure S2a, Supporting Information). After 75 h, the bare Cu electrode voltage hysteresis increased dramatically, and then kept increasing until the system failed. This phenomenon could be ascribed to the repeated growth of Li dendrites.^[28] Figure S3 in the Supporting Information shows the Li plating and stripping performance for the 1st and 125th cycles of Li@MCS900 and Li@Cu electrode at a current density of 1 mA cm⁻². The superiority of the Li@MCS900 electrode can be observed at high current density. At a high current density of 3 mA cm⁻² (Figure 3d), the curve shows that the obvious sharp voltage increase comes out much earlier on bare Cu electrode, and the Li plating/stripping procedure contains serious voltage hysteresis. However, the Li@MCS900 electrode exhibits a very stable and flat Li stripping and plating behavior up to 180 h. This proves the superiority of the nitrogen sites on the framework of MCS900 and how they can homogenize Li ion flow and thus why dendritic formation is slowed. Figure S4 in the Supporting Information reveals the SEM

images before and after Li cycling test on the Li@MCS900 electrode and bare Cu electrode. As shown in Figure S4a in the Supporting Information, the surface of the Cu foil is rugged. After cycling for 100 h at a current density of 1 mA cm⁻², a large number of Li dendrites were observed on the Cu foil electrode (Figure S4b, Supporting Information). When the Cu foil was covered with MCS900, the honeycomb structure of nitrogen-doped carbon spheres was uniformly distributed on the Cu foil (Figure S4c, Supporting Information). Due to the large number of nitrogen sites and large surface area of the sphere, the Li metal can be uniformly plated on Cu foil through the interval of each MCS900 and there is no dendrite formation after 100 h (Figure S4d, Supporting Information).

Coulombic efficiency is a key indicator for assessing the availability of Li during cycling.^[29] As shown in Figure 3e, compared with Li@Cu electrode, the Li@MCS900 electrode exhibits a more stable electrochemical cycling performance and longer lifetime. Specifically, the Li@MCS900 electrode exhibits CE of 96% after 300 cycles at the current density of 1 mA cm⁻². Even at high current density of 3 mA cm⁻², the Li@MCS900 cells still maintain 91% CE after 100 cycles (Figure 3f). In comparison, the Li@Cu cell shows an inferior CE and a shorter lifetime. Although the Li@Cu electrode maintains a stable CE at 1 mA cm⁻² for 50 cycles (Figure 3e), the battery experiences a rapid decay in CE when the current density is increased to 3 mA cm⁻² (Figure 3f). As previously mentioned, the high currents induce undesirable dendrite growth on Cu foil, which damages the SEI layer.

TEM images were employed for further identifying the sulfur distribution inside MCS900 and CMCS1100. As shown in Figure 4a and Figure S5 in the Supporting Information, the sulfur was impregnated into the pores of the MCS900. The

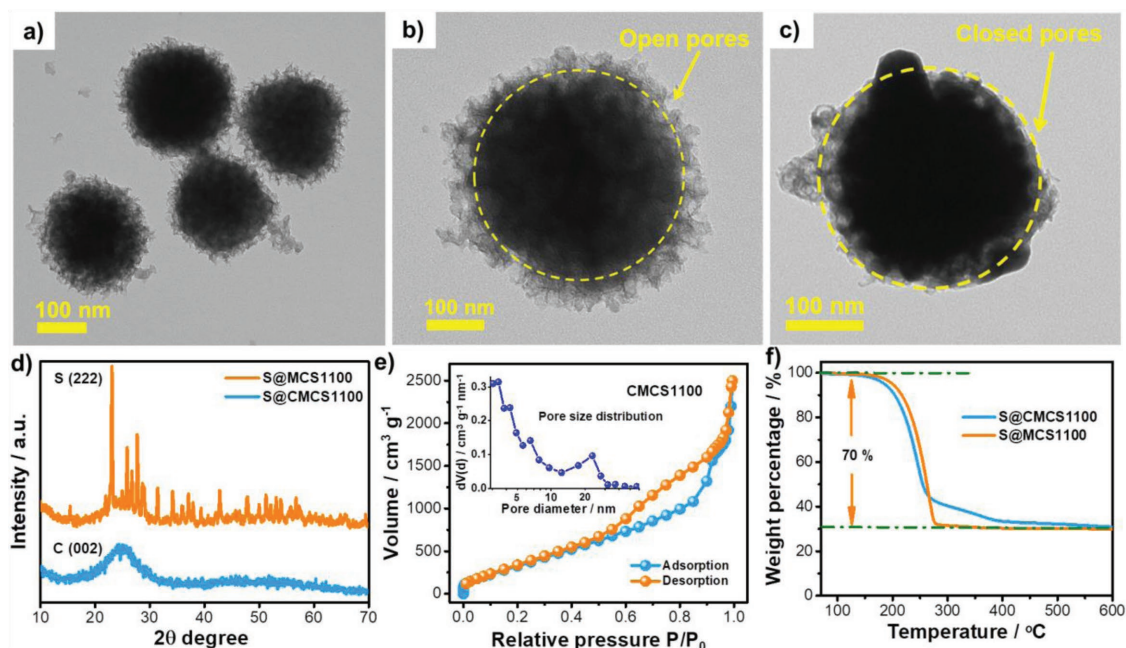


Figure 4. a,b) TEM images of the sulfur-encapsulated MCS900. c) TEM image of the sulfur-encapsulated CMCS1100. d) XRD patterns of S@MCS900 and S@CMCS1100 composites. e) N₂ adsorption–desorption isotherm of S@CMCS1100 composite. The inset is pore size distribution of the CMCS1100. f) TGA curve of S@CMCS1100 in flowing N₂ at a ramp rate of 5 °C min⁻¹.

open porous structure was also observed on the surface of MCS900. For comparison, the obtained S@CMCS1100 composites maintain the sphere morphology and present a uniform sulfur distribution. As shown in Figure 4c, due to the thin layer of carbon wrapping, S@CMCS1100 is much denser than S@MCS900. In addition, the darker area of the CMCS1100 represents heavy sulfur atoms. Some voids still remain in the CMCS1100 materials, which facilitate adaptation to volume changes of sulfur during charge and discharge cycles. Successful loading of sulfur on MCS1100 and CMCS1100 materials is confirmed by XRD and thermogravimetric analysis (TGA). XRD patterns are shown in Figure 4d. For both samples, there is an observable broad diffraction peak at (002). For the S@MCS1100 sample, a large number of sulfur peaks occur due to the open pore structure that cannot encase the sulfur inside. As a result, most of the sulfur will absorb outside of the pore. In contrast, no sulfur peaks are observed for S@CMCS1100 composites, which means that the sulfur has been embedded inside the independently closed carbon cages of the carbon sphere. The surface area and pore size distribution of the CMCS1100 were analyzed by N₂ adsorption–desorption isotherms. As shown in Figure 4e, the isotherms of CMCS1100 presented type IV isotherm characteristics, which indicates the presence of mesopores.^[20] A large BET surface area of 1340 m² g⁻¹ is observed. Pore size distribution revealed mesopores ranging from 2.8 to 20 nm. TGA was performed to determine the content of sulfur in CMCS1100 and MCS1100. As shown in Figure 4f, the content of sulfur in CMCS1100 and MCS1100 is 70 wt% for both. Notably, the diminishing percentage of sulfur observed in CMCS1100 can be attributed to the excellent sulfur confinement.

Figure 5a shows the schematic illustration of the functional role of CMCS1100 material on sulfur in Li–S batteries. The CMCS1100 possesses advantages of high conductivity and effective polysulfide confinement. Furthermore, it can effectively stabilize the shuttle effect of polysulfide when the carbon layer is wrapped on the outer surface. The excellent electrochemical properties of the S@CMCS1100 cathode are attributed to the better electron and ion transport and enhanced reaction kinetics. In order to investigate the Li ion diffusion coefficients (D_{Li}) in the cathodes, cyclic voltammetry (CV) curves at various scan rates were analyzed. According to the Randles–Sevcik equation^[6,30]

$$I_p = (2.69 \times 10^5) n^{1.5} A D_{\text{Li}}^{0.5} C_{\text{Li}} \nu^{0.5} \quad (1)$$

where ν is the sweep rate, I_p is the current of peaks, C_{Li} is the concentration of electrolyte, n is the number of reaction electrons, and A is the electrode area. CV curves of S@CMCS1100 at various sweep rates are shown in Figure 5b, which display the typical peaks of Li–S batteries. The D_{Li} values are obtained from the linear relationship of I_p and $\nu^{1/2}$ ($I_{p-A} = 0.7294\nu^{1/2} + 0.0247$, $I_{p-C} = -0.4755\nu^{1/2} - 0.0889$) in Figure 5c, where $D_{\text{Li}^+ - \text{Cathodic}} = 3.58 \times 10^{-6}$ cm² s⁻¹ and $D_{\text{Li}^+ - \text{Anodic}} = 8.43 \times 10^{-6}$ cm² s⁻¹. Figures S6 and S7 in the Supporting Information are the CV curves of S@MCS1100 cell and S@MCS900 cell obtained at a scan rate of 0.1 mV s⁻¹, respectively.

In order to analyze the charge transfer resistance, the electrochemical impedance spectroscopy (EIS) measurements were performed. Figure 5d shows the Nyquist plots of the S@CMCS1100, S@MCS1100, and S@MCS900 electrodes before other testing. There are two regions present in the EIS curves.

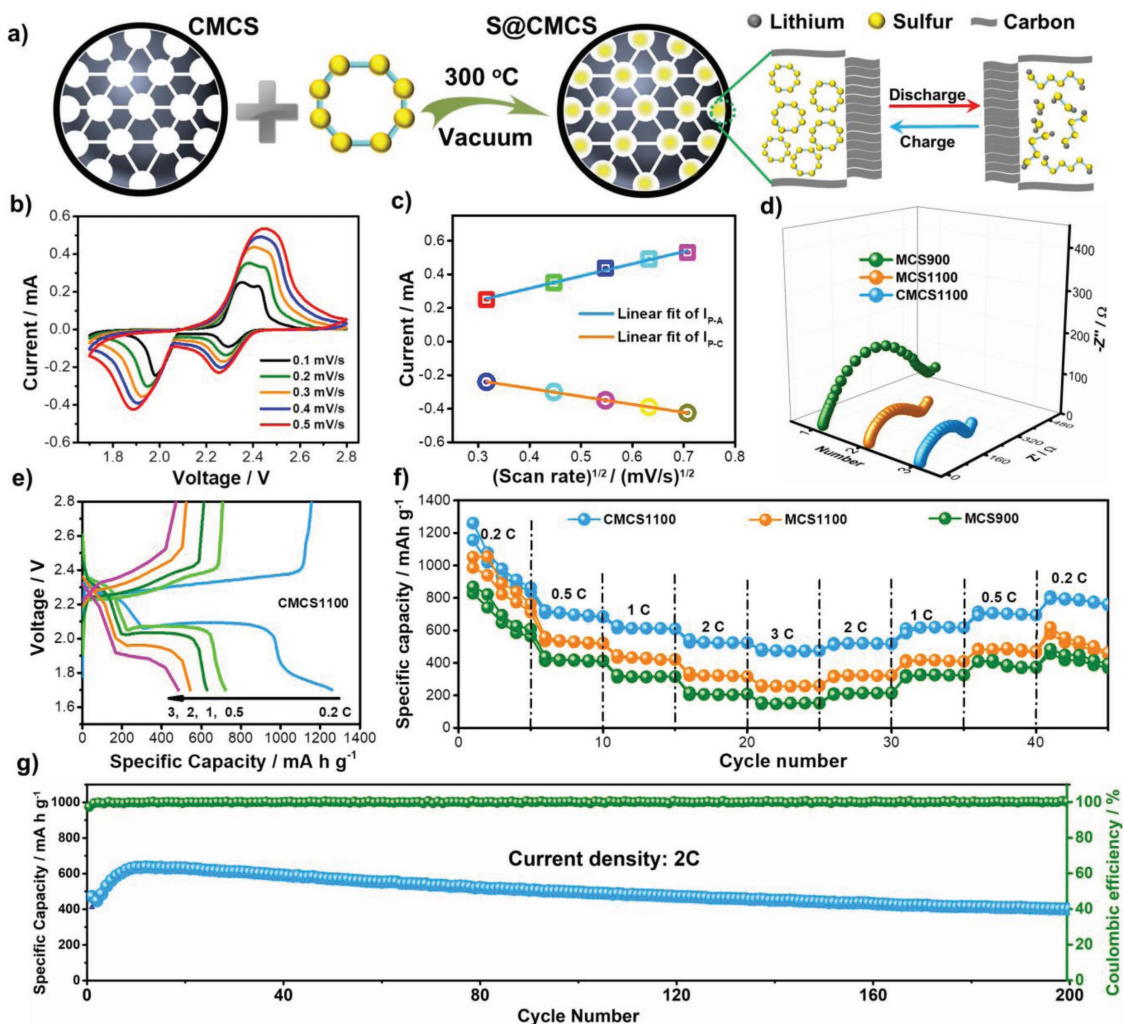


Figure 5. a) Schematic illustration of the mechanisms of sulfur cathode during the charge and discharge processes. b) Cyclic voltammetry of the S@CMCS1100 at scan rates of 0.1, 0.2, 0.3, 0.4, and 0.5 mV s⁻¹. c) Linear relationship of I_p and $v^{1/2}$. d) Nyquist plots of the S@CMCS1100, S@MCS1100, and S@MCS900 before cycling. e) Voltage vs capacity curves at various cycling current densities of the S@CMCS1100 electrode. f) Rate performances of S@CMCS1100, S@MCS1100, and S@MCS900 cells. g) Long-term cycling performance test of the S@CMCS1100 cell at the discharge rate of 2 C.

The first region is the semicircle from high frequency to medium frequency and the second region is the straight line in the low-frequency region.^[2,31] The S@CMCS1100 electrode has a lower charge transfer resistance than the S@MCS1100 and S@MCS900 electrodes, which can be attributed to the improvement in electrical conductivity since sulfur is encapsulated inside the carbon sphere. Figure 5e shows the charge and discharge curves of the S@CMCS1100 electrodes under various dis-/charge rates of 0.2 C, 0.5 C, 1 C, 2 C, and 3 C (1 C = 1675 mA g⁻¹). There are two discharge plateaus found in S@CMCS1100 electrode-based Li-S batteries. The first plateau represents the reduction of S₈ to Li₂S_n ($n > 4$), and the second plateau corresponds to the formation of Li₂S_n ($n \leq 2$) in further reduction process. In the charge profile, the plateau corresponds to the oxidation of Li polysulfide.^[3] Even at high current rates, these plateaus are well maintained, which indicates the electrochemical reaction process with a small barrier.^[32,33] Furthermore, the rate performance of the three cathode materials is evaluated at various current densities (Figure 5f). When

the cell is measured successively at 0.2 C, 0.5 C, 1 C, 2 C, and 3 C, the S@CMCS1100 electrode delivers high stabilized specific capacities of 1260, 723, 628, 544, and 485 mAh g⁻¹, respectively. When the current density goes back to 0.2 C again, the capacity of S@CMCS1100 electrode is recovered to 695 mAh g⁻¹, indicating good stability of the S@CMCS1100 electrode. Compared with S@CMCS1100, the S@MCS1100 and S@MCS900 electrodes have lower capacities at the same current densities. This is attributed to the open pore structure that can cause shuttle effect for the polysulfide during the cycling test. The long-term cycle life of the S@CMCS1100 electrode is tested at a dis-/charge rate of 2 C for 200 cycles (Figure 5g). At 2 C, the S@CMCS1100 electrode delivers a maximum capacity of 411 mAh g⁻¹ and after 200 cycles still maintains a capacity of 400 mAh g⁻¹. The Coulombic efficiency of the S@CMCS1100 cells is >99% during the cycling process. Figure S8 in the Supporting Information shows the schematic illustrations of CMCS1100 and MCS1100 sulfur hosts. The illustrations show the different impacts on

shuttle effect in Li-S batteries. It is evident that the polysulfide in the S@MCS1100 electrode is observable on a large portion of the separator. However, for the S@CMCS1100 electrode, there was much less polysulfide found on the cycled separator. Therefore, the closed porous structure can stabilize the shuttle effect of polysulfide better than the open porous structure.

A full Li-S cell using the stable Li@MCS900 as anode and S@CMCS1100 as cathode was tested to demonstrate the anode's and cathode's excellent electrochemical performances. **Figure 6a** represents a schematic diagram of the full Li-S cell. The CMCS1100 possesses numerous advantages when it is used as a sulfur host. The closed porous structure on the surface of the carbon sphere can effectively encapsulate sulfur inside the independent carbon cages and stabilize the shuttle effect of polysulfide. Additionally, the larger interior volume of the carbon cage can accommodate sulfur species volume expansion during charge and discharge processes. Lastly, CMCS

increases the conductivity and facilitates the Li-ion accessibility. Furthermore, taking Li@MCS900 as the anode, the large surface area and abundant nitrogen sites of MCS900 can effectively guide the Li ion's flow. Therefore, the Li dendrite growth is suppressed during Li plating/stripping process. In **Figure 6b**, the S@CMCS1100 cathode coupled with Li@MCS900 anode shows much higher capacity than S@CMCS1100 cathode coupled with Li@Cu anode. The S@CMCS1100||Li@MCS900 cell achieved stable capacities of 1157 mAh g⁻¹ at 0.2 C, 727 mAh g⁻¹ at 0.5 C, 578 mAh g⁻¹ at 1 C, 475 mAh g⁻¹ at 2 C, and 438 mAh g⁻¹ at 3 C. In comparison, S@CMCS1100||Li@Cu cell revealed capacities of 1032 mAh g⁻¹ at 0.2 C, 628 mAh g⁻¹ at 0.5 C, 434 mAh g⁻¹ at 1 C, 252 mAh g⁻¹ at 2 C, and 192 mAh g⁻¹ at 3 C. This proves that the S@CMCS1100||Li@Cu cell has lower capacities when compared to the S@CMCS1100||Li@MCS900 cell. **Figure 6c** represents the first charge and discharge cycles of S@CMCS1100 cathode coupled with

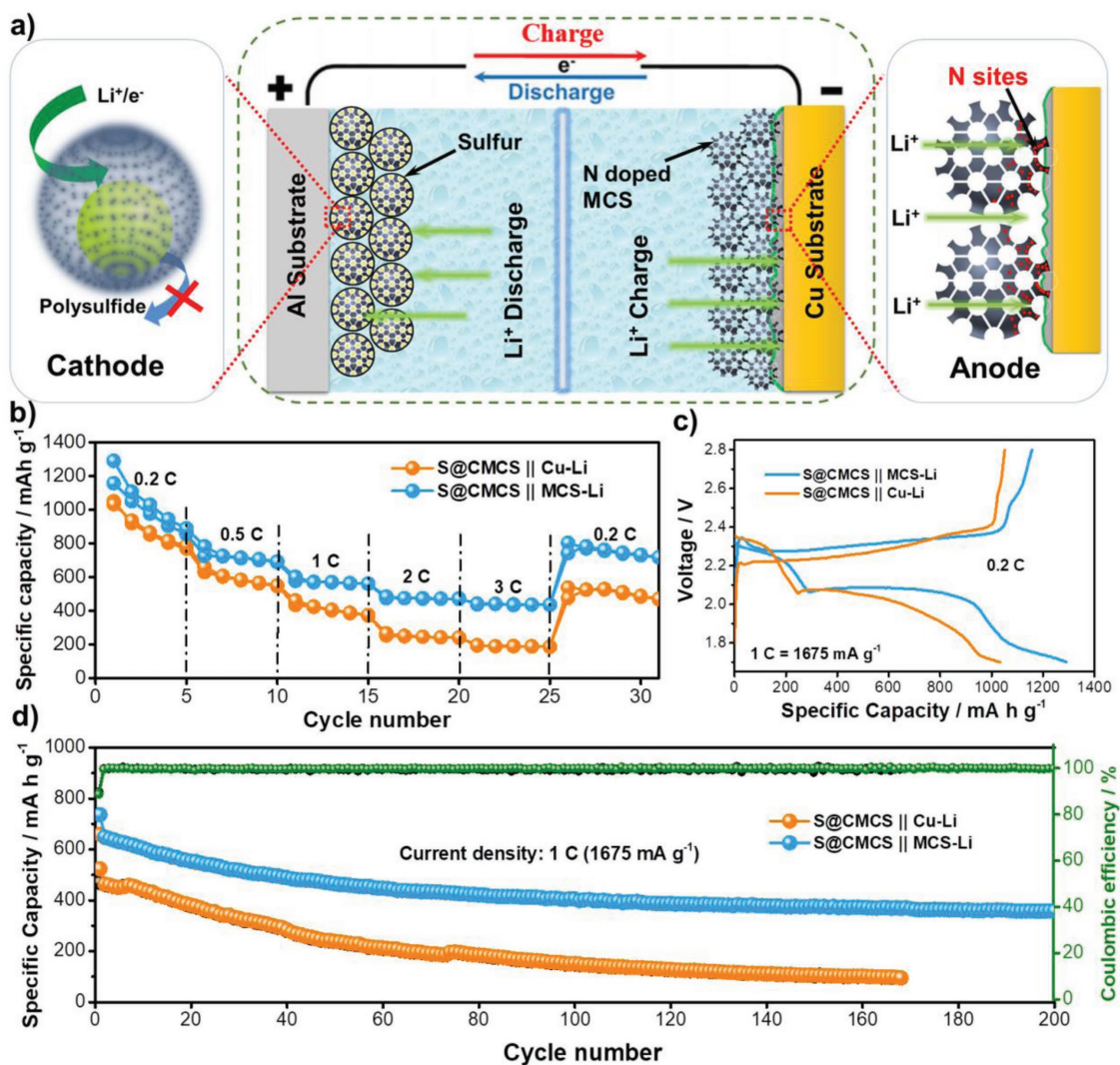


Figure 6. a) Scheme of the full Li-S cell with S@CMCS1100 as cathode and Li@MCS900 as anode. b) Rate performances of S@CMCS1100 cathode coupled with Li@MCS900 anode compared to S@CMCS1100 cathode coupled with Li@Cu anode. c) The first charge/discharge cycles of S@CMCS1100 cathode coupled with Li@MCS900 anode and S@CMCS1100 cathode coupled with Li@Cu anode at current density of 0.2 C. d) Cycling performances of S@CMCS1100 cathode coupled with Li@MCS900 anode and S@CMCS1100 cathode coupled with Li@Cu anode at current density of 1 C for 200 cycles.

Li@MCS900 anode and S@CMCS1100 cathode coupled with Li@Cu anode at 0.2 C. The S@CMCS1100||Li@Cu cell's second plateau is decayed and showed a significant capacity drop. The cycling performance of the Li-S full cell at dis-/charge rate of 1 C was further investigated. At this current rate, the cell can reach up to 200 cycles. As can be seen from Figure 6d, the capacity of S@CMCS1100||Li@MCS900 cell revealed excellent capacity retention rate compared to S@CMCS1100||Li@Cu cell.

3. Conclusions

In conclusion, for the first time, a mesoporous carbon sphere (open pore structure and closed pore structure) was developed utilizing a straightforward but efficient approach. The carbon sphere improved the electrochemical performance of both the sulfur cathode and the Li metal anode for the Li-S batteries. When the MCS900 sample was employed for suppressing Li dendrite growth, the Li@MCS900 electrode delivered excellent cycling stability with more than 350 h and Coulombic efficiency as high as 96% for more than 300 cycles at a current density of 1 mA cm⁻². Even at a higher current density of 3 mA cm⁻², the Coulombic efficiency of Li@MCS900 electrode was still 91% after 100 cycles. Moreover, when CMCS1100 was used as the host for Li-S cathode, it delivered capacities of 411 mAh g⁻¹ at 2 C (3350 mA g⁻¹), and maintained its capacity at 400 mAh g⁻¹ after 200 cycles. Interestingly, a full Li-S battery comprised of MCS900 as anode and CMCS1100 as cathode demonstrated excellent capacity retention. The high reversible capacity and stable electrochemical cycling life are attributed to several reasons. One reason is the MCS900's capability to homogenize the flux of Li ions and inhibit the growth of dendrites due to its honeycomb shape with high surface area and abundant nitrogen sites. Another reason is the ability of the honeycomb structure with one layer of amorphous carbon to encapsulate sulfur and reduce the shuttle of polysulfides. The last reason is that faster electron transfer can occur through the carbon walls of CMCS1100, which improves the stability and rate performance of the Li-S batteries. This work demonstrates the dual-function electrodes with tunable open and closed structures, creating a new concept for developing high energy density Li-S full cells.

Supporting Information

Supporting Information is available from the Wiley Online Library or from the author.

Acknowledgements

H.Z. acknowledges the Northeastern University for tier 1 and start-up support. The authors thank the Kostas Research Institute and Center for Renewable Energy Technology at Northeastern University for the use of SEM, XRD, TEM, etc. The authors also thank the Center for Nanoscale System at Harvard University for using their facilities.

Conflict of Interest

The authors declare no conflict of interest.

Keywords

dendrites, Li metal anodes, Li-sulfur batteries, mesoporous carbon spheres, shuttle effect

Received: November 4, 2018

Revised: December 9, 2018

Published online:

- [1] Q. Pang, A. Shyamsunder, B. Narayanan, C. Y. Kwok, L. A. Curtiss, L. F. Nazar, *Nat. Energy* **2018**, *3*, 783.
- [2] Z. Sun, J. Zhang, L. Yin, G. Hu, R. Fang, H. M. Cheng, F. Li, *Nat. Commun.* **2017**, *8*, 14627.
- [3] R. Fang, S. Zhao, Z. Sun, D. W. Wang, H. M. Cheng, F. Li, *Adv. Mater.* **2017**, *29*, 1606823.
- [4] S. H. Chung, A. Manthiram, *Adv. Mater.* **2018**, *30*, 1705951.
- [5] X. Liang, C. Hart, Q. Pang, A. Garsuch, T. Weiss, L. F. Nazar, *Nat. Commun.* **2015**, *6*, 5682.
- [6] H. Kim, J. Lee, H. Ahn, O. Kim, M. J. Park, *Nat. Commun.* **2015**, *6*, 7278.
- [7] Y. Liu, Q. Liu, L. Xin, Y. Liu, F. Yang, E. A. Stach, J. Xie, *Nat. Energy* **2017**, *2*, 17083.
- [8] Y. Zhong, X. Xia, S. Deng, J. Zhan, R. Fang, Y. Xia, X. Wang, Q. Zhang, J. Tu, *Adv. Energy Mater.* **2018**, *8*, 1701110.
- [9] L. Kong, X. Chen, B. Q. Li, H. J. Peng, J. Q. Huang, J. Xie, Q. Zhang, *Adv. Mater.* **2018**, *30*, 1705219.
- [10] S. H. Chung, K. Y. Lai, A. Manthiram, *Adv. Mater.* **2018**, *30*, 1805571.
- [11] D. Lin, Y. Liu, Z. Liang, H. W. Lee, J. Sun, H. Wang, K. Yan, J. Xie, Y. Cui, *Nat. Nanotechnol.* **2016**, *11*, 626.
- [12] C. P. Yang, Y. X. Yin, S. F. Zhang, N. W. Li, Y. G. Guo, *Nat. Commun.* **2015**, *6*, 8058.
- [13] G. Zheng, S. W. Lee, Z. Liang, H. W. Lee, K. Yan, H. Yao, H. Wang, W. Li, S. Chu, Y. Cui, *Nat. Nanotechnol.* **2014**, *9*, 618.
- [14] J. Zheng, M. H. Engelhard, D. Mei, S. Jiao, B. J. Polzin, J. G. Zhang, W. Xu, *Nat. Energy* **2017**, *2*, 17012.
- [15] Y. Mao, G. Li, Y. Guo, Z. Li, C. Liang, X. Peng, Z. Lin, *Nat. Commun.* **2017**, *8*, 14628.
- [16] L. Liu, Y. X. Yin, J. Y. Li, S. H. Wang, Y. G. Guo, L. J. Wan, *Adv. Mater.* **2018**, *30*, 1706216.
- [17] L. Fan, H. L. Zhuang, W. Zhang, Y. Fu, Z. Liao, Y. Lu, *Adv. Energy Mater.* **2018**, *8*, 1703360.
- [18] R. Zhang, X. R. Chen, X. Chen, X. B. Cheng, X. Q. Zhang, C. Yan, Q. Zhang, *Angew. Chem.* **2017**, *129*, 7872.
- [19] Z. Li, J. Zhang, Y. Lu, X. W. D. Lou, *Sci. Adv.* **2018**, *4*, eaat1687.
- [20] G. Wang, Y. Sun, D. Li, H. W. Liang, R. Dong, X. Feng, K. Müllen, *Angew. Chem., Int. Ed.* **2015**, *54*, 15191.
- [21] Z. Li, J. Zhang, B. Guan, D. Wang, L.-M. Liu, X. W. D. Lou, *Nat. Commun.* **2016**, *7*, 13065.
- [22] H. Li, Y. Hou, F. Wang, M. R. Lohe, X. Zhuang, L. Niu, X. Feng, *Adv. Energy Mater.* **2017**, *7*, 1601847.
- [23] K. Mi, S. Chen, B. Xi, S. Kai, Y. Jiang, J. Feng, Y. Qian, S. Xiong, *Adv. Funct. Mater.* **2017**, *27*, 1604265.
- [24] D. Lin, Y. Liu, Y. Cui, *Nat. Nanotechnol.* **2017**, *12*, 194.
- [25] Y. Liu, D. Lin, Y. Li, G. Chen, A. Pei, O. Nix, Y. Li, Y. Cui, *Nat. Commun.* **2018**, *9*, 3656.
- [26] X. B. Cheng, R. Zhang, C. Z. Zhao, Q. Zhang, *Chem. Rev.* **2017**, *117*, 10403.

- [27] Y. Guo, H. Li, T. Zhai, *Adv. Mater.* **2017**, *29*, 1700007.
- [28] X. Liang, Q. Pang, I. R. Kochetkov, M. S. Sempere, H. Huang, X. Sun, L. F. Nazar, *Nat. Energy* **2017**, *2*, 17119.
- [29] B. D. Adams, J. Zheng, X. Ren, W. Xu, J. G. Zhang, *Adv. Energy Mater.* **2018**, *8*, 1702097.
- [30] J. Liu, T. Qian, M. Wang, J. Zhou, N. Xu, C. Yan, *Nano Lett.* **2018**, *18*, 4598.
- [31] W. Liu, J. Jiang, K. R. Yang, Y. Mi, P. Kumaravadivel, Y. Zhong, Q. Fan, Z. Weng, Z. Wu, J. J. Cha, *Proc. Natl. Acad. Sci. USA* **2017**, *114*, 3578.
- [32] L. Li, L. Chen, S. Mukherjee, J. Gao, H. Sun, Z. Liu, X. Ma, T. Gupta, C. V. Singh, W. Ren, *Adv. Mater.* **2017**, *29*, 1602734.
- [33] H. Du, Z. Zhang, J. He, Z. Cui, J. Chai, J. Ma, Z. Yang, C. Huang, G. Cui, *Small* **2017**, *13*, 1702277.